

**Force of adhesion on supersolvophobic surfaces: The role of capillary necks**

Juan V. Escobar\* and Rolando Castillo

*Instituto de Física, Universidad Nacional Autónoma de México, P.O. Box 20-364, Mexico City 01000, Mexico*

(Received 11 September 2015; revised manuscript received 26 November 2015; published 24 February 2016)

We study theoretically the force of adhesion of pinned liquid drops in contact with supersolvophobic surfaces. We develop a method to calculate the contact and excess surface areas vs compression of the drops against surfaces characterized by an effective interfacial energy in the Cassie-Baxter wetting regime. We find that a  $9^\circ$  difference in contact angle can increase the force of adhesion by almost three orders of magnitude. We investigate the role that the inevitable formation of capillary necks has on this force, which has the same functional form of Derjaguin's result for elastic solids. Our results suggest that measuring the force of adhesion directly on nearly perfectly solvophobic surfaces may be a more precise technique to quantify the effective interfacial energy than traditional contact angle measurements on macroscopic drops.

DOI: [10.1103/PhysRevE.93.022804](https://doi.org/10.1103/PhysRevE.93.022804)**I. INTRODUCTION**

Liquids and solids are in general expected to behave very differently in their contact with a solid surface. Whereas the mechanical deformation of an elastic solid sphere is perfectly reversible [1,2], we know from experience that a liquid drop normally deforms in an irreversible way. Actually, a drop is said to “spread” on a surface, a term that reflects the irreversible nature of the process [3,4]. In other words, wetting phenomena are described by the laws of thermodynamics, whereas mechanics and elasticity theory describe the adhesion between solid objects. Nevertheless, a liquid can behave like a solid under the right circumstances, namely, when it is in contact with a nearly perfect solvophobic surface that makes the contact with the liquid reversible. When this is the case, it has been shown experimentally that a small but finite constant force of adhesion is measured between a macroscopic liquid drop and the solid surface regardless of the history of the compression (Fig. 1) [5]. Indeed, measuring apparent contact angle (CA) on these surfaces is recognized to yield significant experimental errors [6], and using force of adhesion measurements directly is a viable alternative to better quantify the surface-liquid interactions [5,7]. In a recent work, such small interactions were modeled by assuming the CA remains at  $180^\circ$  during the whole process of compression and detachment while allowing a nonzero contact energy term to enter the energy balance [5]. This approach serves as an excellent first approximation to the problem, but it is inherently self-inconsistent because, however small, any surface energy will deviate the CA from perfect solvophobicity, i.e.,  $CA < 180^\circ$ . As a consequence, capillary bridges [8–11] inevitably form during detachment. These bridges are bound to have an effect on the force of adhesion [12,13], despite the fact that on supersolvophobic surfaces (SSSs) they are much smaller than those normally found on solvophilic ones ( $CA < 90^\circ$  [14]). An experimental realization of such a macroscopic system is provided by the contact between liquid mercury on rough diamond surfaces (Fig. 1) that presents an apparent contact angle of  $> 175^\circ$  [5].

In this paper, we study theoretically the force of adhesion between pinned liquid drops of constant volume and SSS (CA between  $170^\circ$  and  $179^\circ$ ), and how its magnitude depends on CA.

To this end, we develop a method to find the profile of a deformed semidrop that makes a constant apparent CA with a wetting surface while being pinned on a backing flat surface possibly connected to a measuring device. From this profile, we obtain the excess surface area of the drop and the contact area of interaction as a function of compression. We then incorporate these terms into a self-consistent energy balance equation of the interaction between the semidrop and the surface in which the apparent CA is related to the thermodynamic contact energy through the Cassie-Baxter model of wetting of rough surfaces [15]. Assuming a fixed grip configuration, we obtain the pull-off force from mechanical stability considerations. We restrict our analysis to drops smaller than the capillary length and slow detachments rates so that both gravitational forces and viscous effects can be neglected. Interestingly, we find that the force of adhesion in the presence of capillary necks has the same functional form as the Derjaguin model of the interaction between elastic solids [1]. We then compare this result to that of a perfectly solvophobic surface that is analogous to the deformation of between a plane and a solid sphere whose profile remains Hertzian [16] at all times. Finally, we use these results to obtain the effective work of adhesion and contact angle directly from the experimental value of the force of adhesion.

Let us first briefly review some properties of adhesion, wetting, and capillary bridges relevant to this paper.

**A. Contact between solids: Adhesion**

Despite the reversibility of the deformation process between elastic solids, when an elastic sphere is compressed and subsequently decompressed from a surface, a finite force is required for its detachment. This force is called force of adhesion or pull-off force  $F_{Ad}^{Solid}$ , and it is the result of a mechanical instability of the system [3,17]. Surprisingly, irrespective of the degree of compliance of the solids or of the range of the interactions involved, this force of adhesion is always proportional to the thermodynamic work of adhesion  $w_a$  and to the radius of the sphere  $r$  [1,2] and is independent

\* Author to whom correspondence should be addressed:  
escobar@fisica.unam.mx

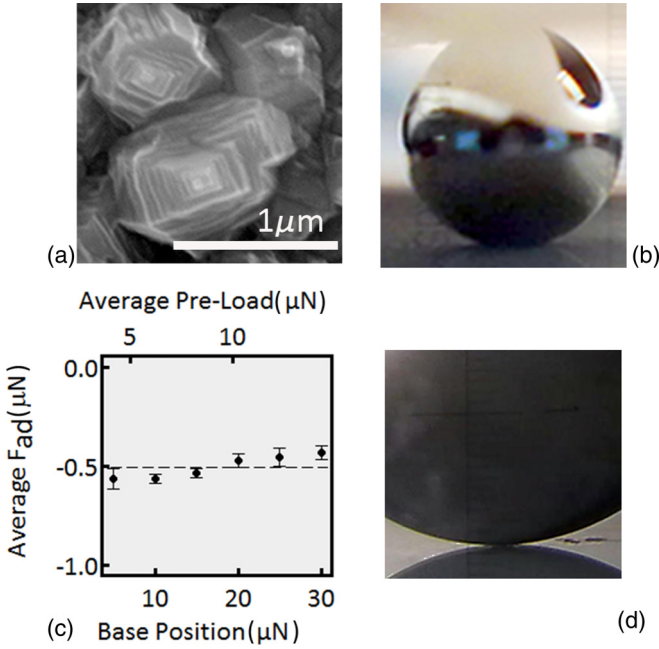


FIG. 1. A supersolvophobic system: Hg on boron-doped diamond. (a) Scanning electron microscopy images of a diamond surface with roughness on two different length scales. (b) A mercury drop resting on this surface. (c) Experimental force of adhesion between a 350 μm radius Hg drop vs preload, Ref. [5]. (d) Hg semidrop being detached from this diamond surface.

of the Young's modulus of either one of the bodies,

$$F_{\text{Ad}}^{\text{Solid}} \propto -r w_a. \quad (1)$$

A thorough review on the various models of the adhesion of solids can be found in Ref. [18] and in the classic work by Maugis [17]. That surface interactions can affect the contact dynamics was realized by Griffith in 1920 [19] in the theoretical description of the propagation of cracks. Later, Maugis [17] extended this approach to the detachment of solids in which the key parameter is the elastic energy release rate  $G$ , the condition for equilibrium is  $G = w_a$ , and the stability criterion is  $(\partial G / \partial A) > 0$ , where  $A$  is the area of contact. An entirely equivalent strategy to obtain the force of adhesion and equilibrium area of contact is to write down the total energy of the system and minimize it with respect to a single parameter that uniquely determines the configuration of the system. This parameter can be, for example, the deformation of the sphere when the experiment is in a constant force configuration as performed in the seminal paper by Johnson-Kendall-Roberts (JKR) [2]. On the other hand, when dealing with experiments in the constant grip configuration, this parameter is the deformation  $\delta$  of the apparatus that provides the nonconstant external force (see Fig. 2). In this case the force is obtained by the product  $(-\delta k)$ , where  $k$  is the spring constant of the apparatus [5,17]. In either case, the total energy  $E_T$  of the system has three components,

$$E_T(\delta) = E_E(\delta) - E_C(\delta) + E_M(\delta), \quad (2)$$

where  $E_C$  is the interaction (contact) energy with the surface (proportional to  $w_a$ ),  $E_M$  is the mechanical energy of the apparatus, and  $E_E$  is the elastic energy stored in the defor-

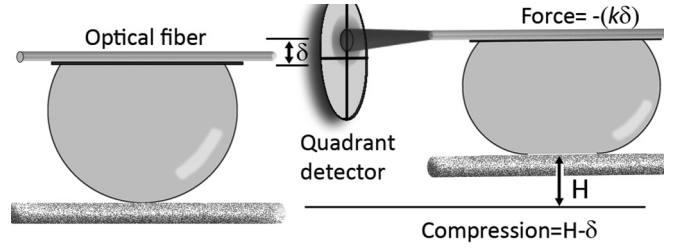


FIG. 2. Constant grip configuration. A base holding a surface is moved a distance  $H$  while an optical fiber with a semidrop of liquid attached to it points to a quadrant detector. As the liquid gets in contact with the surface, the fiber is deflected a distance  $\delta$  [5]. See the Experimental results section.

mation of the sphere. In this context configuration refers only to the particular way in which one chooses to measure the force, and it is not related to the boundary conditions of the physical problem. Remarkably, each configuration gives in general different values of the force of adhesion given the same work of adhesion  $w_a$  [17].

In the case of a spring,  $E_M(\delta) = \frac{1}{2}k\delta^2$ . Reversibility is reflected on the fact that  $E_T$  is a function of  $\delta$  only, and the equilibrium configuration is found by minimizing the total energy  $(\partial E_T / \partial \delta)_H = 0$ . Here,  $H$  is the position of a surface that moves against the sphere (or drop) as shown in the diagram of Fig. 2 so that the compression of the sphere is  $x = (H - \delta)$ . Thus, for an externally imposed  $H$ , the system is completely defined by the equilibrium  $\delta$ . Finally, as the sphere is pulled away from the surface, there will be a point in which the system becomes unstable, and the sphere detaches. This happens when the mechanical equilibrium criterion ceases to hold, i.e., when  $(d^2 E_T / d\delta^2)_H < 0$ . The force supplied at this point is  $F_{\text{Ad}}^{\text{Solid}}$ , and this force is what is measured in adhesion or ‘‘tack’’ experiments in a constant grip configuration.

## B. Wetting of superhydrophobic surfaces

The starting point to study wetting phenomena in general is Young's relation [3,4],

$$\gamma = \gamma_{\text{SV}} - \gamma_{\text{LV}} \cos \theta_E, \quad (3)$$

which gives the equilibrium contact angle  $\theta_E$  between a liquid and a flat homogeneous surface as a function of the surface tensions ( $\gamma_{\text{SL}}$ ,  $\gamma_{\text{SV}}$ , and  $\gamma_{\text{LV}}$ ) of all three phases involved (solid-liquid, solid-vapor, and liquid-vapor, respectively). In both the fields of contact mechanics and wetting, the interfacial energy  $w_a$  (or work of adhesion) is defined as the reversible amount of work that one needs to supply to the system to separate a unit area of contacting liquid from the solid. This definition along with Young's relation yields the Dupr e equation,

$$w_a = \gamma_{\text{LV}}(1 + \cos \theta_E). \quad (4)$$

Thus, knowing the surface tension of the liquid and the equilibrium contact angle, one can infer the interfacial energy. A method known to enhance the wetting properties of a surface is to increase its roughness. There exist two thermodynamic states that define the apparent contact angle  $\theta^*$  on rough surfaces. In the so-called ‘‘Wenzel's’’ state [20], the system minimizes its free energy when the liquid conforms to

the surface profile, which happens on originally solvophilic systems (resulting in  $\theta^* < \theta_E$ ) and on moderately solvophobic ones (resulting in  $\theta^* > \theta_E$  [21]). In contrast, surface roughness can increase the apparent contact angle ( $\theta^* > \theta_E$ ) of originally solvophobic ones, creating what is called a Cassie-Baxter state [15]. In this case, the contact angle measured on the rough surface is given by

$$\cos \theta^* = -1 + \phi_s(1 + \cos \theta_E), \tag{5}$$

where  $\phi_s < 1$  is the fractional surface area with which the liquid is in actual contact.  $\phi_s$  is a crucial parameter in this wetting state since the contact angle increases because the liquid is progressively more in contact with air than with the surface itself. As long as the liquid remains flat in-between the supporting protrusions [22], it is possible to assign to the rough surface an effective work of adhesion  $w_a^e$  that is reduced in proportion to  $\phi_s$ ,

$$w_a^e = \phi_s w_a. \tag{6}$$

Equation (6) makes it possible to study supersolvophobic systems as if it were composed of a liquid in contact with a flat surface with energy  $w_a^e$ . Combining Eqs. (4)–(6), we arrive at  $w_a^e = \gamma_{LV}(\cos \theta^* + 1)$ , which after dividing by  $w_a$  becomes

$$\phi_s = (w_a^e/w_a) = (\gamma_{LV}/w_a)(\cos \theta^* + 1). \tag{7}$$

Figure 3 shows  $\phi_s$  (left axis) as obtained with Eq. (7) as a function of  $\theta^*$  for a range of supersolvophobic states for the Hg-diamond system shown in Fig. 1 for which  $\theta_E = 155^\circ$  [5]. This figure illustrates the nonlinear effect that surface roughness has on  $\theta^*$ : If one wanted to increase  $\theta^*$  from  $170^\circ$  to  $179.9^\circ$ , then  $\phi_s$  would have to decrease by three orders of magnitude. Although it may seem at first glance that by reducing  $\phi_s$  any  $\theta^*$  could be obtained, having too small a  $\phi_s$  can make the Cassie-Baxter state unstable with respect to pressure changes and transition to a Wenzel one [21]. This general lack of robustness is why it is so difficult to study superhydrophobic systems experimentally.

The Hg-diamond system mentioned above is actually robust in this sense, in part because the equilibrium CA on a flat diamond surface is unusually high to begin with. Using Eq. (4) and  $\gamma_{LV} = 486.5 \text{ mJ m}^{-2}$  for Hg gives  $w_a = 45.6 \text{ mJ m}^{-2}$ , and as a result, a relatively modest value of  $\phi_s = 1/25$  is

capable of yielding  $\theta^* > 175^\circ$  [5]. The right axis of Fig. 3 shows the effective interfacial energy for this system in a Cassie-Baxter state. For reference, a very small surface energy of  $w_a \cong 2 \text{ mJ m}^{-2}$  exists in the contact between native silicon oxide and gold immersed in ethanol [23]. If the surface in question is not only rough, but also composed of structures on both the micro and the nanoscales [24], then it is possible to achieve apparent loss of macroscopic contact angle hysteresis [3,4,24,25]. Under these circumstances it is found that the force of adhesion of a macroscopic drop of Hg ( $\sim 0.5\text{-mm}$  radius) is independent of the history of the compression (or preload, Fig. 1(c) [5]), just as in the case of elastic solids. Actually, loss of contact angle hysteresis can also be achieved in nanoscopic systems [26]. This phenomenon is theoretically predicted to happen when the contact points between the liquid and the solid constitute “weak” pinning points of the contact line, a term coined by de Gennes *et al.* [4] and Joanny and de Gennes [25]. In the presence of weak pinning points the force of adhesion between a liquid drop and a solid surface can be calculated following the same formalism summarized in the previous section about the contact between solids since in the absence of hysteresis the energy balance is a function of the parameter  $\delta$  only [5]. To be able to use Eq. (2), the elastic energy  $E_E$  of the solid needs to be replaced by the energy contribution coming from the increase in the excess surface area  $a_{ex}$  of the compressed liquid drop. Here, we call this energy “pseudoelastic,”  $E_{PE} = a_{ex}\gamma_{LV}$  since it gives rise to a restoring force. Thus, to calculate the force of adhesion in a supersolvophobic system, one needs to obtain first the dependence of both the surface and the contact areas of the compressed drop as a function of  $\delta$  (see Fig. 2). In a previous work [5], the energy balance was approximated by assuming that the profile of the drop is given by a perfectly hydrophobic contact (CA =  $180^\circ$ ) at all times, while allowing a small interfacial contribution  $E_C$ , limited to the contact area  $A_C$ , to enter the energy balance. This is equivalent to the Derjaguin [1] model of the contact between an elastic sphere and a plane that always makes a Hertzian contact during compression and subsequent decompression [16]. Although this model serves as a good first-order approximation, note that it is inherently self-inconsistent because in the contact between liquids and solids, even the smallest interaction energy will decrease the contact angle below  $180^\circ$ . In order to construct a self-consistent approach to describe this interaction, we propose a model in which  $\theta^*$  is a function of  $w_a^e$  as given by Eq. (7), whereas the contact energy is proportional to this same energy  $w_a^e$ . Allowing CA  $\neq 180^\circ$  means that capillary bridges will be present that will be particularly narrow due to the supersolvophobic nature of the surfaces. Indeed, the profile of liquid surfaces can present abrupt deformations because the flexural rigidity of their surfaces is practically zero [27], i.e., as long as the surface area is minimized, there is no energetic cost of deforming the surface, however sharp the deformation may be. This case is unlike that of liquid crystals or cell membranes for which it is necessary to consider Helfrich’s energy [28].

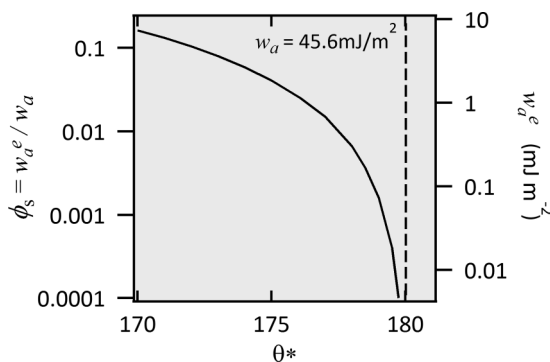


FIG. 3. Fractional surface area  $\phi_s$  (left axis) and effective interfacial energy (right axis) vs  $\theta^*$  for the Cassie-Baxter model assuming  $w_a = 45.5 \text{ mJ m}^{-2}$  (Hg-diamond system).  $\theta^*$  spans the apparent contact angles of the supersolvophobic systems.

**C. Capillary bridges**

Capillary bridges are axisymmetric liquid junctions between two solids, and they play an important role in the

adhesion of biological [29] and granular [30] systems as well as in the adhesion between man-made microstructures [31]. For example, water condensation can lead to capillary bridges in antiferromagnetic adhesion tests that can result in a substantial increase in the force of adhesion in the contact mode [32] and influence the general dynamics of the cantilever in tapping mode [33]. A thorough review on the subject of capillary bridges can be found in Ref. [11]. From a theoretical point of view, capillary bridges between planar surfaces have been studied before at constant contact angles [14,34–36] or pinned on both surfaces [36,37]. In this paper, we study mixed boundary conditions since we consider a drop pinned to a surface as it is compressed, stretched, and detached from a surface with which it makes a constant apparent CA (Fig. 2). We have chosen these particular boundary conditions because they match those encountered in the laboratory [5], thus allowing our results to be compared to experiments on SSSs. In order to obtain the mechanical properties of one of these solid-liquid-solid systems, it is necessary to know the profile of the capillary bridge. In the case of solvophilic surfaces, several approximations can be made that allow finding analytical solutions [11]. One such assumption usually made is the so-called “toroidal” approximation that considers that the profile of the liquid is given by a portion of a circle. However, this clearly does not hold in the case of SSSs for which the derivative of the profile has an inflection point as will be shown in Fig. 6(a). Therefore, the Young-Laplace axisymmetric equation [4] must be solved without any approximations given the boundary conditions of the problem. These solutions allow for the formation of bridges that, due to their very small relative size on SSSs, we henceforth call capillary necks instead. In the following section, we develop a model to solve for the profile of a semidrop that meets the boundary conditions mentioned above. We find that, however small they may be, capillary necks have a strong effect on the force of adhesion.

**II. THEORETICAL MODEL OF THE DEFORMATION OF A SEMIPINNED DROP**

In this section, we present a method to obtain both the contact and surface areas as a function of compression of a drop that wets a supersolvophobic surface while being pinned on a backing substrate that holds it. The general strategy we follow to find the profile of the deformed drop is to patch together the positive and negative branches of the solution of the differential equation that gives this profile at the point of zero derivative. We do this while keeping the volume constant and meeting the corresponding boundary conditions imposed by  $\theta^*$  on the wetting surface and by the position of the pinned contact line on the backing surface.

Consider a sessile liquid drop of radius  $r$  pinned on a backing surface with which it makes a contact angle  $\theta_p$  as shown schematically in Fig. 4(a) for the particular case of  $\theta_p = 120^\circ$ .  $\theta_p$  is the initial contact angle, which will change as the drop is compressed and stretched. Assume that the drop is smaller than the capillary length (i.e., gravity can be neglected) so that energy minimization of the surface yields a truncated circular profile  $y(z)$ . For purposes of integration, it is actually more convenient to define  $\theta_p$  by specifying the value of the parameter  $\varepsilon$  that determines the range by which

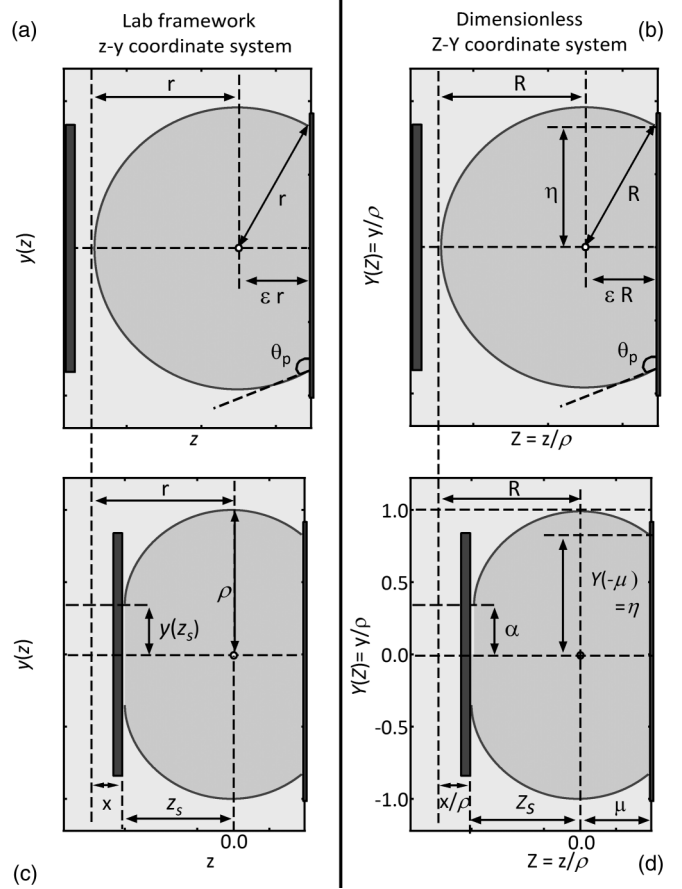


FIG. 4. Coordinate systems and variables. Profile in the  $z = y$  coordinate system (left panel) of the drop pinned at a backing surface ( $\theta_p = 110^\circ$ ), before [top (a)] and after [bottom (c)] compression against a perfectly solvophobic surface ( $\theta^* = 180^\circ$ ). The equivalent profiles are shown in the dimensionless  $Z$ - $Y$  coordinate system for the uncompressed (b) and compressed drop (d). Note that both  $z$  and  $Z$  axes increase towards the left.

the profile is extended from the point of zero derivative of the profile to the backing surface [Fig. 4(a)]. This parameter is always in the range of  $\{-1, 1\}$ , and values of  $(\theta_p)$  greater, equal, or smaller than  $90^\circ$  are achieved when  $(\varepsilon)$  is positive, zero or negative, respectively. The volume and area of this undeformed drop are  $v_s = (2/3)\pi r^3(1 + 3\varepsilon/2 - \varepsilon^3/2)$  and  $a_s = 2\pi r^2(1 + \varepsilon)$ , respectively. These quantities are important because the volume of the drop must be conserved while its excess surface area multiplied by the surface tension gives the pseudoelastic energy contribution to the energy balance. To find the profile  $y(z)$  of the deformed drop we need to minimize its surface area while keeping its volume constant. Since the shape of the drop is axisymmetric, the surface area is given by  $a = 2\pi \int y(z)\sqrt{1 + [\partial_z y(z)]^2} dz$ , whereas the volume is  $v = \pi \int y(z)^2 dz$ . If  $\lambda$  is a Lagrange multiplier, then  $y(z)$  is an extremal of the functional,

$$f = 2\pi \int F[z, y(z), y'(z)] dz = 2\pi \gamma_{LV} \left( \int \{y(z)\sqrt{1 + [\partial_z y(z)]^2}\} dz - \frac{\lambda}{2} \int y(z)^2 dz \right). \tag{8}$$

Since  $F(z)$  does not depend explicitly on the variable  $z$ , it is possible to use Euler's first integral directly,  $C = y' \partial_y F(z) - F(z)$ , where  $C$  is a constant of integration. Solving for  $y'(z)$ ,

$$y'(z) = \pm \sqrt{\frac{4\gamma_{LV}^2 y(z)^2}{[-2C + \lambda y(z)^2]^2} - 1}. \quad (9)$$

Unlike other problems pertaining to the calculus of variations with constraints, the parameter  $\lambda$  cannot be solved as an analytical function of the volume of the drop. Nevertheless, it is possible to conserve volume by hand while simultaneously imposing the boundary conditions. To do this, first note in Figs. 4(a) and 4(c) that the drop is pinned to the backing surface, and therefore, the height of the profile is fixed, but the slope will vary as the drop is compressed. In contrast, the contact angle against the wetting surface is fixed, but the position of the line will depend on the compression precisely because volume has to be conserved. Thus, we are dealing with mixed boundary conditions. We get around this problem by calculating all the relevant quantities in a new coordinate system in which the boundary conditions are met

naturally and introducing scaling rules to recover the value of these quantities in the laboratory framework. We begin by incorporating the boundary conditions into the differential equation itself. As illustrated in Fig. 4(c), let  $y(z_s)$  be the contact point of the compressed profile of the drop on the wetting surface. At that point, the slope  $y'(z_s) \equiv \xi$  of the profile gives the contact angle  $CA = (180^\circ/\pi)\text{arccot}(\xi)$ , which is to remain fixed. This first boundary condition can be imposed on Eq. (9) leading to

$$C = -\frac{\lambda y^2(z_s)}{2} + \frac{\gamma_{LV} y(z_s)}{\sqrt{1 + \xi^2}}. \quad (10)$$

Then, let  $\rho$  be the maximum height of the profile which is set to happen at  $z = 0$ , and let  $d$  be the derivative at that point [i.e.,  $y'(0) \equiv d$  and  $y(0) \equiv \rho$ ]. Note that if  $\theta_p > 90^\circ$  (the case studied here), then  $\rho > r$  and vice versa, and that in the case that  $\theta_p \geq 90^\circ$ ,  $d$  is necessarily zero, i.e., there exist a maximum of the profile of the drop. This condition yields

$$\lambda = \frac{2\gamma_{LV}\rho}{\rho^2 - y(z_s)^2} \left(1 - \frac{y(z_s)}{\rho\sqrt{1 + \xi^2}}\right). \quad (11)$$

The constant  $\lambda$  is actually the pressure difference inside the drop with respect to the pressure outside, usually written as a function of both the first and second derivatives of  $y(z_s)$  [4]. Substituting the expressions for  $C$  and  $\lambda$  back in the differential equation for the profile yields

$$y'(z) = \pm \sqrt{\frac{[\rho^2 - y(z_s)^2]^2 y^2(z)}{\{y(z_s)[y^2(z) - \rho^2](1 + \xi^2)^{-1/2} + \rho[y(z_s)^2 - y^2(z)]\}^2} - 1}. \quad (12)$$

Equation (12) can be rewritten in dimensionless form as

$$Y'(Z) = \pm \sqrt{\frac{(1 - \alpha^2)^2 Y^2(Z)}{\{\alpha[Y^2(Z) - 1](1 + \xi^2)^{-1/2} + [\alpha^2 - Y^2(Z)]\}^2} - 1}, \quad (13)$$

where  $Z \equiv z/\rho, Y \equiv y/\rho, \alpha \equiv Y(Z_s) = y(z_s)/\rho$ , and  $Z_s \equiv z_s/\rho$ . Writing the differential equation for the profile in this way is very useful since the only boundary condition necessary to solve for the profile is  $Y(0) = 1$ . Note that the dimensionless variables  $Z$  and  $Y$ , actually constitute a new coordinate system (CS)  $Z$ - $Y$  (right panel, Fig. 4). Once all the relevant quantities have been obtained in the  $Z$ - $Y$  CS, it is necessary to translate them into the original  $z$ - $y$  one since this is the laboratory framework. To accomplish this task, note that if an area or a volume are calculated in this  $Z$ - $Y$  CS, we only need to multiply such a quantity by  $\rho^2$  or  $\rho^3$ , respectively, to get its value in the original  $z$ - $y$  CS. This property will come in handy when imposing that the volume of the deformed drop be conserved. Analogously, any quantity proportional to the radius  $r$  of the original semisphere in the  $z$ - $y$  CS is recovered by multiplying its value in the  $Z$ - $Y$  system by  $\rho$ , which serves as a scaling parameter. In particular, the drop's radius is  $r = R\rho$ , where  $R$  is the radius of the uncompressed drop in the dimensionless CS [see Fig. 4(b)]. Our dimensionless analysis is somewhat similar to that of Fortes [36], but it differs from it in that our scaling parameter  $\rho$  is not fixed *a priori* by the boundary conditions of the drop in the  $z$ - $y$  CS. We now consider the

pressure inside the drop, which must remain constant for all  $Z$ 's. Written in terms of the boundary conditions, the pressure difference [Eq. (11)] takes the following dimensionless form in the  $Z$ - $Y$  CS,

$$\Pi \equiv \lambda \left(\frac{\rho}{\gamma_{LV}}\right) = \frac{2}{(1 - \alpha^2)} \left(1 - \frac{\alpha}{\sqrt{1 + \xi^2}}\right). \quad (14)$$

Note that for any given  $\alpha$ ,  $\Pi$  has a maximum when  $\xi = 0$ , which corresponds to a normal contact with the wetting surface (or  $\theta^* = 90^\circ$ ). This case is equivalent to the JKR model for solids [2]. In contrast, for a perfectly solvophobic contact for which  $\xi = -\infty$  (or  $\theta^* = 180^\circ$ ),  $\Pi$  has a minimum, and it reduces to Laplace's pressure for an uncompressed drop of semicircular profile ( $2\gamma_{LV}/r$  in the  $z$ - $y$  CS) when  $\alpha = 0$ .

Equation (13) can be recast in terms of  $\Pi$  only as

$$Y'(Z) = \pm \sqrt{\frac{Y^2(Z)}{\{1 + (\Pi/2)[Y^2(Z) - 1]\}^2} - 1}. \quad (15)$$

The boundary conditions on the wetting surface given by  $\alpha$  and  $\xi$  fully determine  $\Pi$  [Eq. (14)] and with it, the profile of the whole drop through Eq. (15). Since  $\Pi$  must be constant

for all  $Z$ , both branches of Eq. (15) are necessary to obtain the profile of the drop. Note that this mathematically correct because  $\Pi$  is constant and both branches must meet the same boundary condition at the cusp, namely,  $Y(0) = 1$  and  $Y'(0) = 0$ . Physically, using both branches is justified because Eq. (15) does not depend explicitly on  $Z$  and, therefore,  $Y(Z)$  is invariant under an inversion of the coordinate  $Z \rightarrow -Z$ . Using this equation as a starting point, we now develop a method to find all relevant quantities in this CS and to translate them back into the laboratory framework.

First, we characterize any given surface by some apparent contact angle  $\xi$  (or equivalent  $\theta^*$ ). Then, for some value of  $\alpha > 0$ , the dimensionless pressure  $\Pi$  is calculated [Eq. (14)], and the profile of the drop is obtained numerically [Eq. (15)]. This solution yields numerically the point  $Z_S$ , defined as the distance from the contact point against the surface to the abscissa of the cusp. Figure 4(d) shows an example of the deformed profile obtained in the dimensionless  $Z$ - $Y$  CS, whereas the corresponding profile of the original uncompressed drop is depicted in Fig. 4(b) in this same CS. The equivalent profiles in the laboratory framework are shown in Figs. 4(a) and 4(c). As explained above, in both Figs. 4(c) and 4(d), the negative branch of the solution for  $Y'(Z)$  is used to extend the profile of the curve from its cusp to the backing surface by an amount  $\mu > 0$ , which must be determined from the condition of conservation of volume in this CS while simultaneously imposing that the contact line be pinned at the baking surface. Actually, note that, since the drop is pinned, fixing  $\mu$  necessarily determines the height of the profile  $\eta$  where it meets the backing surface [Fig. 4(d)],

$$\eta = Y(-\mu). \quad (16)$$

This point of constant height also serves as a reference to find the radius  $R$  of the original drop in the  $Z$ - $Y$  CS, which is calculated by considering the geometric relation evident from Fig. 4(b),

$$R = \frac{\eta}{\sqrt{1 - \varepsilon^2}}. \quad (17)$$

Then, the parameter  $\mu$  is chosen by inspection to meet the condition of constant volume,

$$\begin{aligned} \pi \int_0^{Z_S} Y(Z)^2 dZ + \pi \int_{-\mu}^0 Y(Z)^2 dZ \\ = \frac{2}{3} \pi R^3 (1 + 3\varepsilon/2 - \varepsilon^3/2), \end{aligned} \quad (18)$$

with arbitrary accuracy. Equation (18) ensures that the volumes of the compressed [Fig. 4(d)] and uncompressed drop [Fig. 4(b)] are equal while keeping the line pinned. The surface area is then calculated (also numerically) for that value of  $\mu$  as

$$\begin{aligned} A_S = 2\pi \int_0^{Z_S} Y(Z) \sqrt{1 + [\partial_Z Y(Z)]^2} dZ \\ + 2\pi \int_{-\mu}^0 Y(Z) \sqrt{1 + [\partial_Z Y(Z)]^2} dZ. \end{aligned} \quad (19)$$

Note that  $A_S$  gives the area in the  $Z$ - $Y$  CS, but we are interested in the area as measured in the laboratory framework, which is simply  $a_S = (A_S \rho^2)$ . Also, since the only length scale

of the problem is the radius of the drop  $r$ , it is convenient to write down all relevant quantities in dimensionless form rescaling them by  $r$ . In particular, the area of the undeformed drop in the original  $z$ - $y$  CS is rescaled by the cross-sectional area of the sphere as

$$\tilde{a}_S \equiv \frac{a_S}{2\pi r^2} = \frac{A_S}{2\pi} \left( \frac{\rho^2}{r^2} \right). \quad (20)$$

Recalling that  $r = R\rho$ , Eq. (17) implies that  $(\rho/r)^2 = (1 - \varepsilon^2)/\eta^2 = R^{-2}$ , which yields an expression for the scaled area in the  $z$ - $y$  CS that is a function of  $\eta$  only,

$$\tilde{a}_S = A_S \left( \frac{1 - \varepsilon^2}{2\pi \eta^2} \right). \quad (21)$$

Note that rather than  $\tilde{a}_S$  itself, what is ultimately relevant for the energy balance is the scaled *excess* surface area  $\tilde{a}_{ex}$ ,

$$\tilde{a}_{ex} \equiv \tilde{a}_S - \frac{2\pi r^2(1 + \varepsilon)}{2\pi r^2} = A_S \left( \frac{1 - \varepsilon^2}{2\pi \eta^2} \right) - (1 + \varepsilon). \quad (22)$$

On the other hand, the contact area ( $A_C$ ) with the wetting surface is  $(\pi\alpha^2)$  in the  $Z$ - $Y$  CS, and it is transformed into the  $z$ - $y$  one and rescaled as

$$\tilde{a}_C \equiv \frac{a_C}{2\pi r^2} = \frac{\rho^2 A_C}{2\pi r^2} = \alpha^2 \frac{1 - \varepsilon^2}{2\eta^2}. \quad (23)$$

Finally, the actual compression in the  $Z$ - $Y$  CS is  $X \equiv (x/\rho) = R(1 + \varepsilon) - (Z_S + \mu)$  [see Figs. 3(b) and 3(d)], which is rescaled by  $r$  and transformed back into the  $z$ - $y$  CS as

$$\tilde{x} \equiv (X\rho)/r = x/r = (1 + \varepsilon) - (Z_S + \mu) \frac{\sqrt{1 - \varepsilon^2}}{\eta}. \quad (24)$$

We stress the point that all the quantities ( $\eta$ ,  $Z_S$ ,  $A_S$ , and  $\alpha$ ) used in the expressions of the scaled excess area [Eq. (22)], contact area [Eq. (23)], and compression [Eq. (24)] are uniquely determined by the value of  $\mu$  chosen to conserve volume, given certain  $\varepsilon$  (or equivalently,  $\theta_p$ ) and certain contact slope  $\xi$  (or equivalently,  $\theta^*$ ). The corresponding contributions to the total energy in the laboratory framework are the contact energy,

$$E_{\text{contact}} \equiv E_C = 2\pi r^2 (w_a^e \tilde{a}_C), \quad (25)$$

and the surface energy,

$$E_{\text{surface}} \equiv E_{PE} = 2\pi r^2 (\gamma_{LV} \tilde{a}_{ex}), \quad (26)$$

where the subscript ‘‘PE’’ means ‘‘pseudoelastic’’ since it is related to a restoring force. Finally, the actual pressure difference in the laboratory CS can be recovered from the relation,

$$\Delta P \equiv \lambda = \Pi \frac{\eta}{\sqrt{1 - \varepsilon^2}} \left( \frac{\gamma_{LV}}{r} \right). \quad (27)$$

In the cases in which  $\theta_p < 90^\circ$  (a ‘‘shallow’’ semidrop) the exact same method applies with the only difference that the limits of the integrals of Eqs. (18) and (19) change, and Eq. (15) must be modified to incorporate the fact that  $d \neq 0$ .

Specifically, the condition to conserve volume reduces to

$$\pi \int_{-\mu}^{Z_S} Y(Z)^2 dZ = \frac{2}{3} \pi R^3 (1 + 3\varepsilon/2 - \varepsilon^3/2), \quad (28)$$

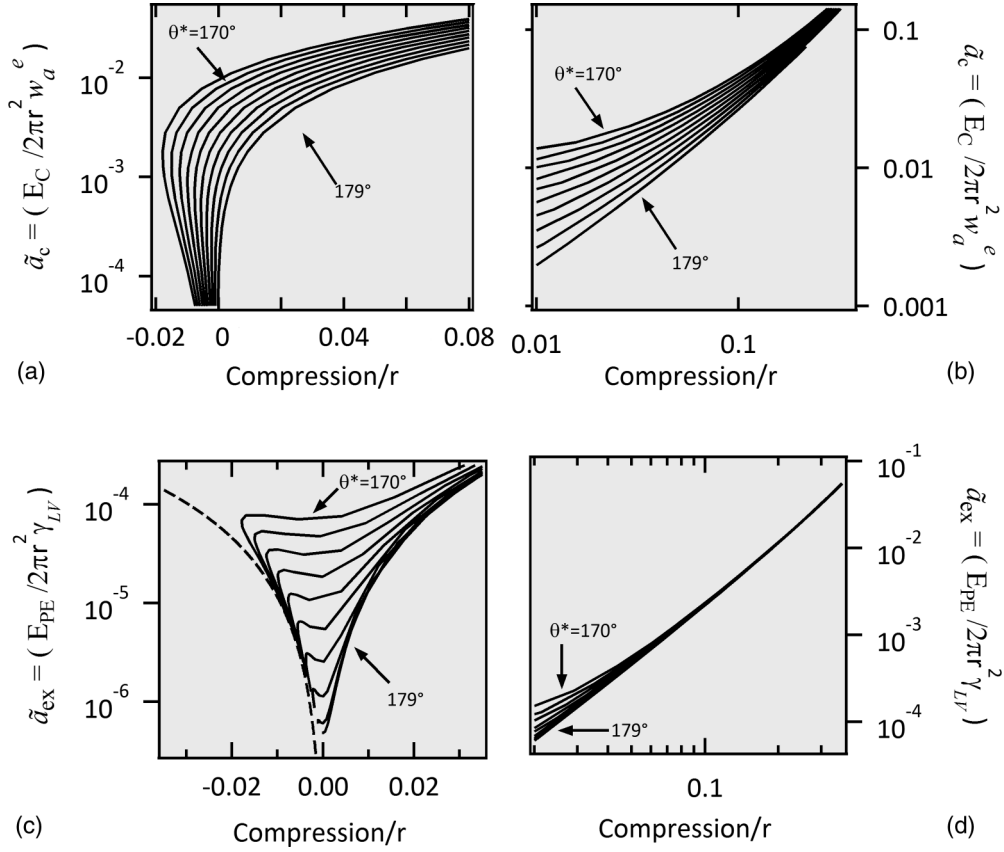


FIG. 5. Results: supersolvophobic surfaces. (a) Scaled contact area vs scaled compression for  $\theta_p = 110^\circ$  and different values of  $\theta^* = \{179^\circ, 178^\circ, \dots, 171^\circ, 170^\circ\}$ . The negative values of the compression signal the appearance of capillary necks. (b) The same as in (a) but for larger positive compressions and on a logarithmic scale. (c) Scaled excess surface area vs scaled compression for the same parameters. The dashed line denotes the function  $\tilde{a}_{ex} \propto \bar{x}^2$ , that follows well the limiting behavior of all curves towards zero compression. (d) The same as (c) but on a logarithmic scale and for larger positive compressions.

whereas the surface area becomes

$$A_S = 2\pi \int_{\mu}^{Z_S} Y(Z) \sqrt{1 + [\partial_Z Y(Z)]^2} dZ. \quad (29)$$

### III. RESULTS AND DISCUSSION

#### A. Adhesion on supersolvophobic surfaces and capillary necks: Numerical results

As an application of the method developed in the previous section, superhydrophobic systems with  $\theta^* = \{179^\circ, 178^\circ, 177^\circ, \dots, 171^\circ, \text{ and } 170^\circ\}$  were investigated for the specific case of  $\theta_p = 110^\circ$ . For each combination of  $\theta^*$  and  $\theta_p$ , the following procedure is followed. First, a value of  $\alpha > 0$  is chosen (ranging from  $\alpha = 0.01$  to  $\alpha = 0.6$ ), which along with  $\xi$  determines  $\Pi$  [Eq. (14)]. This allows solving the differential equation of the profile [Eq. (15)] with the boundary condition  $Y(0) = 0$ . Then, the key quantity  $\mu$  is found so that volume is conserved [Eq. (18)] within  $10^{-10}\%$ . The compression is then obtained indirectly with Eq. (24). Figures 5(a) and 5(b) show  $\tilde{a}_c$  whereas Figs. 5(c) and 5(d) show  $\tilde{a}_{ex}$  vs  $\bar{x}$  (on different scales for better appreciation) for the various SSSs studied. The relationships displayed in these figures give all the relevant mechanical properties of the drop-surface system that will be used to calculate the pull-off force. In particular, note that as

the drop is retracted, the compression reaches negative values, i.e., the drop is being stretched. This signals the appearance of capillary necks. Figure 6(a) shows the profile of one of these necks for the particular case of  $\theta^* = 170^\circ$ . Note the slope of the profile changes close to contact to meet the surface at the required  $\theta^*$ . Even though the profile of Fig. 6(a) seems perfectly spherical, it is actually not. If it were, it would be impossible to have simultaneous capillary necks and satisfy a constant Laplace's pressure all throughout the profile. Indeed, we have verified that the profiles obtained correspond to surfaces of constant mean curvature.

Since capillary necks form during the detachment process, they are bound to have an effect on the pull-off force as opposed to the case of perfectly solvophobic systems for which the profile of the drop always meets the surface at  $180^\circ$  as we will show in the next section. We identify three different stages of the mechanical behavior of the drop during its compression and stretching on different supersolvophobic surfaces. Figures 6(b)–6(d) show more clearly the characteristics of these three stages. For large relative compressions, there exists a power law relationship between  $\tilde{a}_{ex}$  and  $\tilde{a}_c$  [Fig. 6(b)] that is similar to that found for a perfectly solvophobic system (Fig. 11, next section). This first stage lasts until the compression is zero as shown in the example for  $\theta^* = 170^\circ$  in Fig. 6(d). As stretching begins, the contact area decreases at

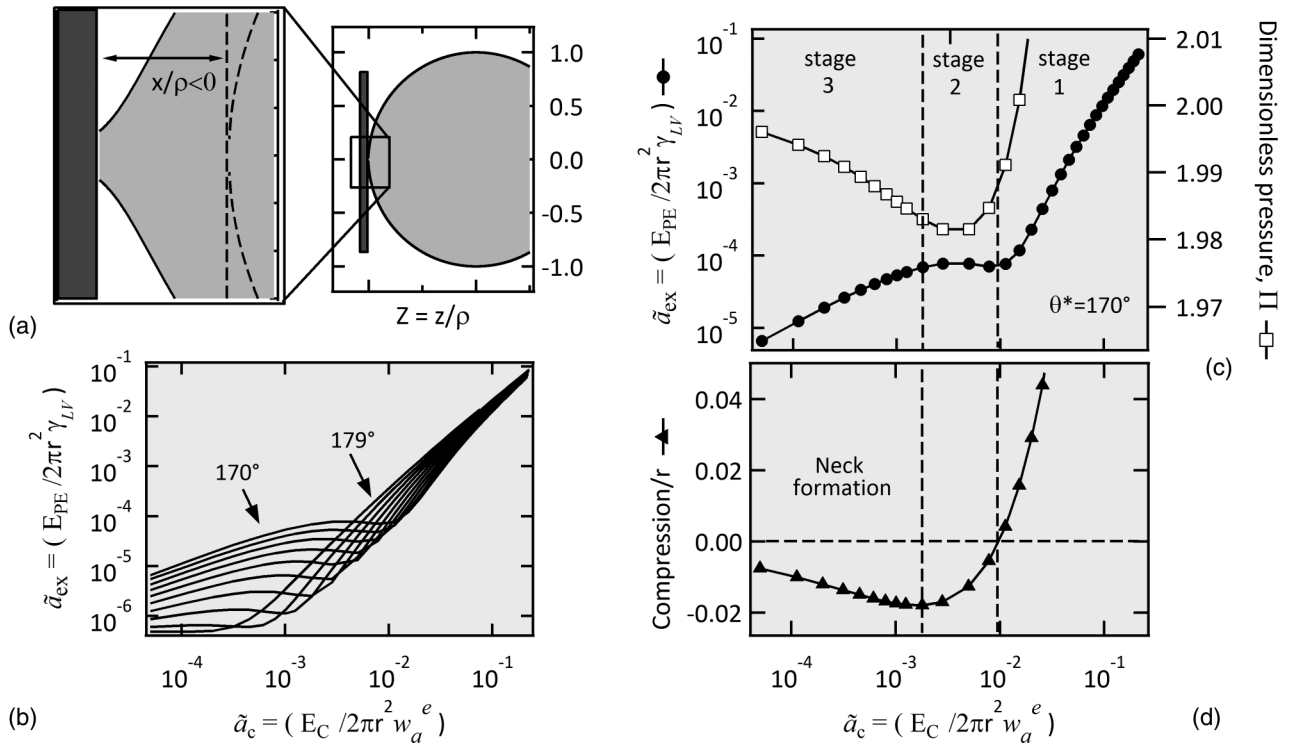


FIG. 6. Capillary neck formation. (a) Profile of a semidrop with  $\theta_p = 110^\circ$  being stretched during detached from a surface with  $\theta^* = 170^\circ$ . The inset shows the formation of a neck when the compression becomes negative, and the circular dashed line shows the profile of the original uncompressed drop. In the case shown, the negative compression corresponds to  $(x/r) = -0.01$ . (b)  $\tilde{a}_{ex}$  vs  $\tilde{a}_c$  for the different supersolvophobic cases studied. (c)  $\tilde{a}_{ex}$  (left axis) and  $\Pi$  (right axis) vs  $\tilde{a}_c$  for the case of  $\theta^* = 170^\circ$  showing the three different stages of the mechanical behavior for the deformation of a drop. (d) Dimensionless compression  $\tilde{x}$  vs  $\tilde{a}_c$ . Neck formation begins when  $\tilde{x}$  reaches a minimum.

almost constant surface area. During this stage (stage 2), the dimensionless pressure reaches a minimum. This stage ends when the compression reaches its maximum negative value. After this point (stage 3), the dimensionless pressure increases [Fig. 6(c)], and the surface area decreases again for smaller contact areas. At this stage, capillary necks are stretched until detachment occurs. The mechanical characteristics of the capillary necks at this stage will determine the pull-off force. As mentioned in the Introduction, this force is determined by the mechanical stability of the system that nonetheless will be a function of the effective thermodynamic work of adhesion  $w_a^e$ . Upon instability, the neck will break and give way to a stable configuration of lower total energy.

Whereas in the case of the adhesion between solids this new configuration of lower energy simply consists of the solid sphere no longer in contact with the plane, and this is not necessarily the case for liquid drops since the drop may break in two, transferring some liquid to the contacting surface. This is a particularly likely scenario in solvophilic systems where the energy of the two-drop system will depend on the volume of the liquid transferred. SSSs present an advantage in this sense because the energetic cost of leaving a small drop behind will always be much higher than that of full detachment. This is a consequence of the fact that the contact area is many orders of magnitude smaller than the surface one (Fig. 7, left axis) because of the very large apparent contact angles involved. This effect is accentuated further in the Hg-diamond system by the two order of magnitude difference between the surface

tension  $\gamma_{LV}$  and the effective work of adhesion (Fig. 7, right axis). As a result, when calculating the total energy of the system composed of the pinned semidrop and the transferred drop, the contact term can be neglected. Given that the sum of the areas of these two spheres is necessarily larger than that of a single semidrop of the same combined volume, a detachment devoid of any transferred liquid yields the lowest possible energy, just as in the case of elastic solids. This lowest

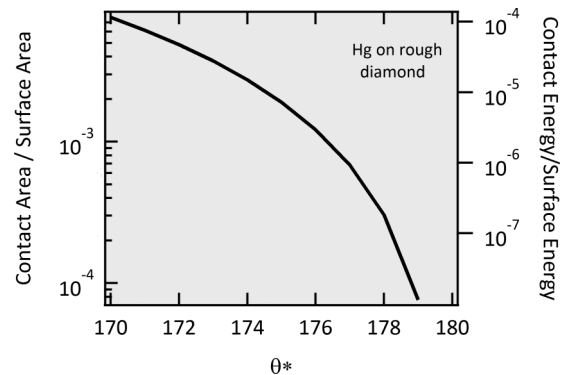


FIG. 7. Areas ratio. (Left) Ratio of contact area and surface area vs  $\theta^*$  for a sessile semidrop on a supersolvophobic surface. (Right) The same ratio but multiplied by  $w_a^e/\gamma_{LV}$ , yielding the ratio of the corresponding energies for the  $\theta^*$  for the diamond-Hg system. The effective energy  $w_a^e$  is calculated for each  $\theta^*$  using Eq. (7).

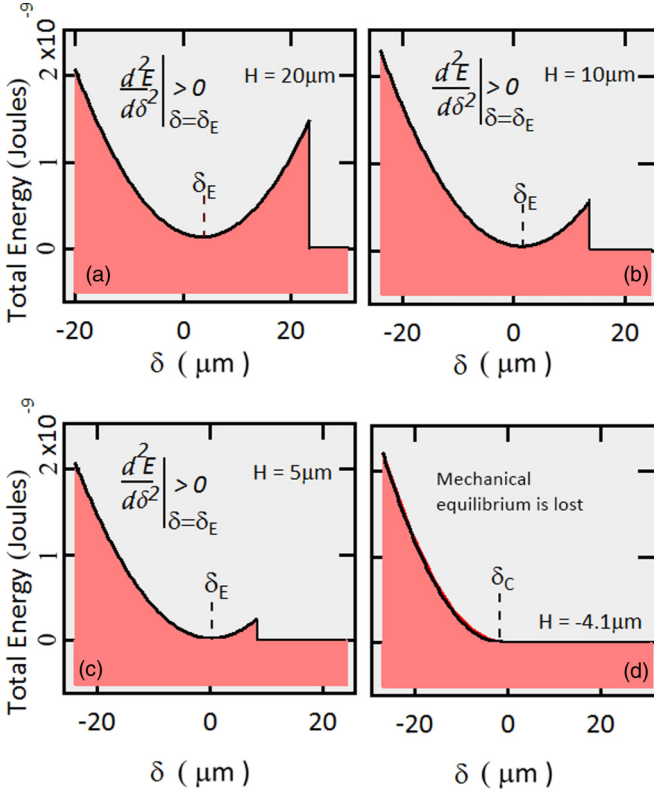


FIG. 8. Mechanical instability and force of adhesion. Total energy vs  $\delta$  for a Hg semidrop of radius  $R = 350 \mu\text{m}$  in contact with a diamond surface with  $\theta^* = 173^\circ$  ( $w_a^e = 3.6 \text{ mJ m}^{-2}$ ) and  $\theta_p = 110^\circ$  for different base heights  $H$ : (a)  $20 \mu\text{m}$ , (b)  $10 \mu\text{m}$ , (c)  $5 \mu\text{m}$ , and (d)  $-4.12 \mu\text{m}$ . In (d), the mechanical instability yields a force equal to  $F_{ad} = k\delta_c$ . In this example,  $k = 5.4 \text{ N m}$ .

energy value is actually zero because  $\tilde{a}_{ex}$ ,  $\tilde{a}_c$ , and  $\tilde{x}$  are all zero for that configuration.

Keeping this in mind, we can now write down the total energy of the system [Eq. (2)] and perform the mechanical stability analysis (see Fig. 8). Recall that since we are dealing with a fixed grip configuration, our goal is to find the deflection  $\delta$  of the measuring device that minimizes the energy and to assess the stability of the system at that point. The total energy of the system is obtained by adding the contact [Eq. (25)] and pseudoelastic [Eq. (26)] contributions to the mechanical term  $\frac{1}{2}k\delta^2$ ,

$$E_T = E_{PE} - E_C + E_M \\ = 2\pi r^2[\gamma_{LV}\tilde{a}_{ex}(\tilde{x}) - w_a^e\tilde{a}_c(\tilde{x})] + \frac{1}{2}k\delta^2, \quad (30)$$

where  $\tilde{a}_{ex}$  and  $\tilde{a}_c$  are functions of  $\tilde{x} = (x/r) = (H - \delta)/r$ . For any given base displacement  $H$ , the total energy can then be calculated as a function of  $\delta$ , given the parameters  $\gamma_{LV}$ ,  $w_a^e$ ,  $k$ , and  $r$ , and the values of  $\tilde{a}_{ex}$  and  $\tilde{a}_c$  shown in Fig. 5. As an example of the evolution of energy landscape as a function of  $\delta$ , Fig. 8 shows the total energy of the system calculated with Eq. (30) for a supersolvophobic system similar to that investigated in recent experiments [5], namely, a  $350 \mu\text{m}$  radius semidrop of Hg ( $\theta_E = 155^\circ$ ) on a diamond surface with  $\theta^* = 173^\circ$  and  $k = 5.4 \text{ N m}$  for different values

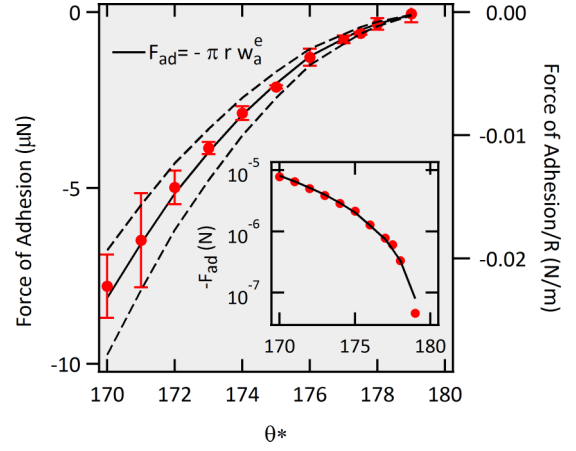


FIG. 9. Results: calculated force of adhesion vs  $\theta^*$ . (Left axis) Calculated force of adhesion vs  $\theta^*$  for a  $350 \mu\text{m}$  radius Hg semidrop with  $\theta_p = 110^\circ$  on a diamond surface. (Right axis)  $F_{ad}/r$  vs  $\theta^*$ . The solid line depicts a force of adhesion equal to  $-\pi r w_a^e$ . The dashed lines correspond to  $-(5/6)\pi r w_a^e$  and  $-(6/5)\pi r w_a^e$  (see the text). The error bars are the uncertainty due to the finite number of sampling points (finite number of  $\alpha$ 's). The inset: absolute value of  $F_{ad}$  (dots) and  $F_{ad} = \pi r w_a^e$  (solid line) vs  $\theta^*$  on a log-linear scale.

of  $H$ . Recall that  $\theta^*$ ,  $w_a^e$ , and  $\theta_E$  are all related to each other through Eqs. (2) and (3) (Cassie-Baxter model). The equilibrium deflection of the measuring device ( $\delta_E$ ) is that which minimizes the energy at constant  $H$  while satisfying the aforementioned condition of stability,  $(d^2 E_T/d\delta^2)_H > 0$ . In Figs. 8(a)–8(c),  $H$  is positive, which corresponds to a compression, and the equilibrium is stable. But as the base is retracted and stretching of the drop begins, there is a position for which the minimum no longer corresponds to a point of zero derivative [Fig. 8(d)]. In other words, the equilibrium condition ceases to hold, i.e.  $(dE_T/d\delta)_H \neq 0$  for all  $\delta$ . Note this situation is different than the case where an equilibrium point exists, but it becomes mechanically unstable  $(d^2 E_T/d\delta^2)_H < 0$ . Mechanical equilibrium ceases to exist at a critical deflection  $\delta_c$ , and the force at this point is the pull-off force or force of adhesion  $F_{ad} = (-k\delta_c)$ . The force of adhesion obtained in this way is shown in Fig. 9 as a function of  $\theta^*$  for the  $350 \mu\text{m}$  semidrop of Hg on a diamond surface. Since a finite number of values of  $\alpha$  is sampled, there exists an uncertainty in the exact value of the critical deflection. Therefore,  $\delta_c$  is chosen as the average between the two closest points to the minimum, and an uncertainty equal to half the distance between those points is ascribed to each value of the force of adhesion. The calculated  $F_{ad}$  (dots) along with the corresponding uncertainties (bars) is plotted in Fig. 9. The force of adhesion is well fit (solid line, Fig. 9) to

$$F_{ad} = -\pi r w_a^e. \quad (31)$$

Note that Eq. (31) is independent of  $\gamma_{LV}$ . The dashed lines in Fig. 9 depict two limiting curves given by  $-(5/6)\pi r w_a^e$  and  $-(6/5)\pi r w_a^e$ . Given the present uncertainty, these two curves serve as a confidence interval for the best fit to the data. Equation (31) is the exact same expression as to that obtained from the Derjaguin model for the adhesion of solids in the

constant grip configuration [17]. However, it is worth pointing out that whereas in the contact between solids the force of adhesion is independent of Young's moduli of the bodies, the force of adhesion given by Eq. (31) does depend on the surface tension of the liquid through  $w_a^e$  [Eqs. (4) and (6)]. Note in the inset of Fig. 9, that  $F_{ad}$  changes by more than two orders of magnitude between the two extremes of the apparent angles examined, namely, between  $\theta^* = 170^\circ$  and  $179^\circ$ . Provided an apparatus capable of measuring the force of adhesion between a liquid drop and a plane on this scale [5], measuring  $F_{ad}$  directly may provide a better estimate of  $w_a^e$  than measuring  $\theta^*$  directly. We provide an example of this method in the experimental Sec. III C.

We realize that data presented in Fig. 9 is calculated for the specific case of  $\theta_p = 110^\circ$ , and  $F_{ad}$  may vary for different values of  $\theta_p$ . Nevertheless, this force of adhesion influenced by capillary necks is already more than three times larger than that obtained using the approximation of a perfectly solvophobic system with the same  $\theta_p$  as we show in the next section. Before moving on to the next section, we would like to point out the limits of the validity of this model. We are assuming that the macroscopic angle  $\theta^*$  is constant throughout the whole compression and subsequent detachment process. For this to hold, a relatively large number  $N$  of subareas must be in touch with the liquid at the moment of detachment, i.e., the surface should still look rough relative to the dimension of the neck. For the experimental case under discussion ( $\theta^* > 175^\circ$  [5]), our model predicts that the liquid is in contact with a couple of tens of subareas of size  $6.6 \times 10^{-2} \mu\text{m}^2$  at the moment of detachment. Therefore, the Cassie-Baxter model still applies, and  $\theta^*$  can be considered as constant, but we are close to the limit of validity. Nevertheless,  $N$  increases steeply for smaller values of  $\theta^*$ .

### B. Adhesion on perfectly solvophobic surfaces

A perfectly solvophobic surface is one that forms a  $\theta^*$  of  $180^\circ$  with the liquid drop, which in reality is impossible to achieve since even the smallest surface energy will deform the contact line, thus creating a neck upon detachment. Nevertheless, examining this case is illustrative as it is analogous to the Derjaguin model of the contact between solids in which the deformation of the sphere is always Hertzian. Furthermore, in this case, the functional form of the corresponding energy contributions vs compression makes it possible to obtain an analytical solution of the force of adhesion as we show next. Figure 10 shows  $\tilde{a}_{ex}$  and  $\tilde{a}_c$  vs  $\tilde{x}$  for the perfectly solvophobic interaction for different values of  $\theta_p$ . Note that when  $\theta^*$  is strictly  $180^\circ$ , the compression always remains positive, and, therefore, there is no capillary neck, as expected. This fact can be appreciated further in Fig. 11 in which we plot  $\tilde{a}_{ex}$  vs  $\tilde{a}_c$ : The surface area decreases monotonically with the contact area, regardless of how small the latter is. Figure 11 is to be contrasted with Fig. 6(b) for the supersolvophobic case. For small compressions, the dimensionless excess surface [Fig. 10(b)] and contact [Fig. 10(d)] areas are very well fit to

$$\tilde{a}_{ex} = S_o \tilde{x}^\beta, \quad (32)$$

and

$$\tilde{a}_c = A \tilde{x}^2 + B \tilde{x}. \quad (33)$$

Unlike the case of the supersolvophobic surfaces, here the surface and contact energies are univalued functions of the compression, and this fact allows us to write down Eq. (2) explicitly as a function of  $H$  and  $\delta$ , that are straightforward to differentiate. The total energy for the perfectly-solvophobic

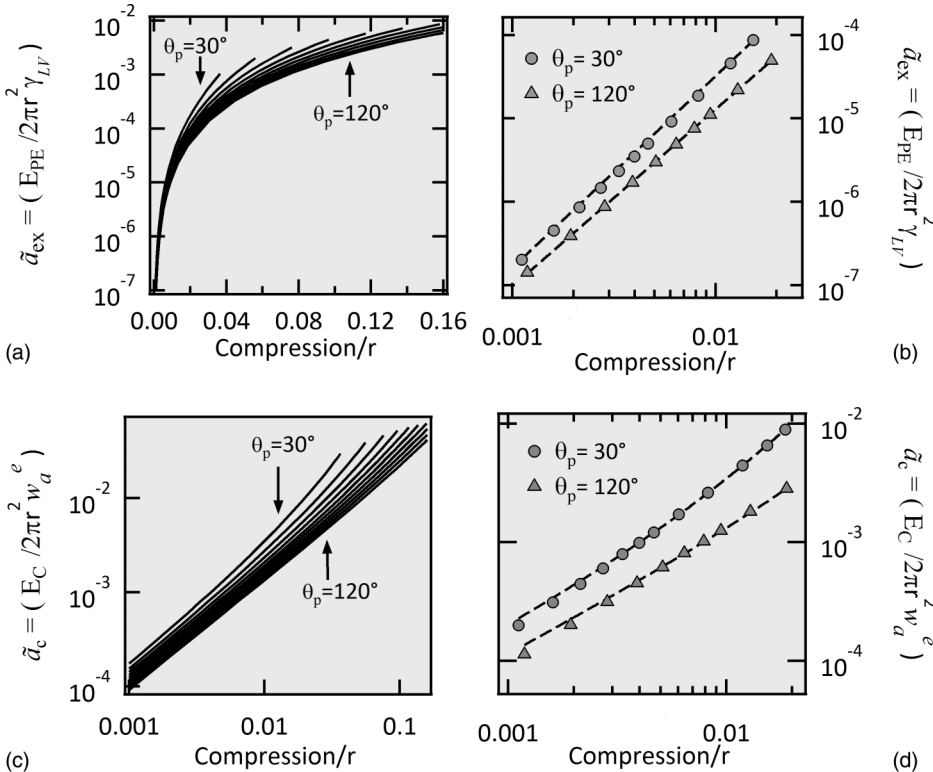


FIG. 10. Results: perfectly solvophobic surface. (a) Scaled excess surface area vs scaled compression for consecutive values of  $\theta_p$  starting at  $30^\circ$  (b) the same as in (a) but only for  $\theta_p = 30^\circ$  and  $120^\circ$  and on a log-log scale for small compressions ( $\tilde{x} < 0.02$ ). The dashed lines are the best fits to Eq. (32),  $\tilde{a}_{ex} = S_o \tilde{x}^\beta$  with  $\{\beta = 2.3, S_o = 1.28\}$  for  $\theta_p = 30^\circ$  and  $\{\beta = 2.1, S_o = 0.23\}$  for  $\theta_p = 120^\circ$ . (c) Dimensionless contact area vs compression. (d) The same as in (c) but only for  $\theta_p = 30^\circ$  and  $120^\circ$  and on a log-log scale also for small compressions. The dashed lines are the best fits to Eq. (33),  $\tilde{a}_c = A \tilde{x}^2 + B \tilde{x}$  with  $\{A = 15.8, B = 0.19\}$  for  $\theta_p = 30^\circ$  and  $\{A = 2.04, B = 0.11\}$  for  $\theta_p = 120^\circ$ .

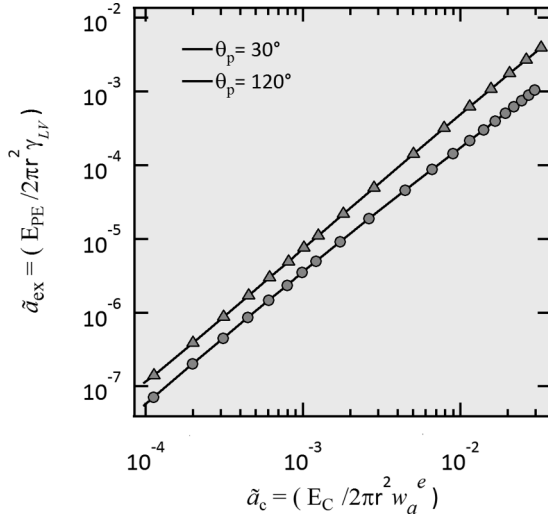


FIG. 11. Results: perfectly solvophobic surface. Dimensionless surface energy vs scaled contact energy for  $\theta^* = 180^\circ$ .

system is as follows:

$$E_T = 2\pi r^2 \gamma_{LV} [(H - \delta)^\beta S_0 - 2\pi r^2 w_a^e [(H - \delta)^2 A + (H - \delta)B] + \frac{1}{2} k \delta^2]. \quad (34)$$

Unlike the SSS case, here it is in principle possible to obtain the force vs compression relation by calculating  $(\partial E_T / \partial \delta)_H = 0$  and solving for  $\delta_E$ . The same applies to the stability criterion. Unfortunately, given the particular values of the exponent  $\beta$  found, it is impossible to arrive at an algebraic expression for the force of adhesion. However, an excellent approximation can be obtained if the exponent is replaced by  $\beta = 2.5$ .

In this case, a rather lengthy but algebraic expression for the equilibrium deflection  $\delta$  (not shown) as a function of the position of the base  $H$  can be found from the condition  $(dE_T / d\delta)_H = 0$ . This deflection  $\delta(H)$  becomes a complex number (i.e., a real solution ceases to exist) when

$$R^2 \gamma_{LV}^6 S_0^6 (Hk + 2B\pi R w_a^e)^3 \times \left\{ -4k^3 R + 48Ak^2 \pi R w_a^e + 2\pi^3 R w_a^e \right. \\ \left. \times [675B\gamma_{LV}^2 S_0^2 + 128A^3 (w_a^e)^2] \right. \\ \left. + 3k\pi^2 [225H\gamma_{LV}^2 S_0^2 - 64A^2 R (w_a^e)^2] \right\} = 0. \quad (35)$$

Solving for  $H$ , we obtain the critical position of the base  $H_c$  at which point the drop detaches from the surface. This critical position of the base is  $H_c = -2B\pi r w_a^e / k$ . Substituting back into the expression for  $\delta$  obtained from the condition  $(dE_T / d\delta)_H = 0$ , the corresponding critical deflection of the measuring device is  $\delta(H_c) \equiv \delta_c = -2B\pi r w_a^e / k$ , yielding the approximate force of adhesion,

$$F_{ad} = -2B\pi r w_a^e. \quad (36)$$

Since  $H_c = \delta_c$ , the compression is zero, and therefore, the contact area at the moment of detachment is also zero. This happens analogously to the detachment of a solid elastic sphere from a plane in the Derjaguin model [1]. Once again, note that  $F_{ad}$  is independent of  $\gamma_{LV}$  and of  $S_0$ , just as it is independent

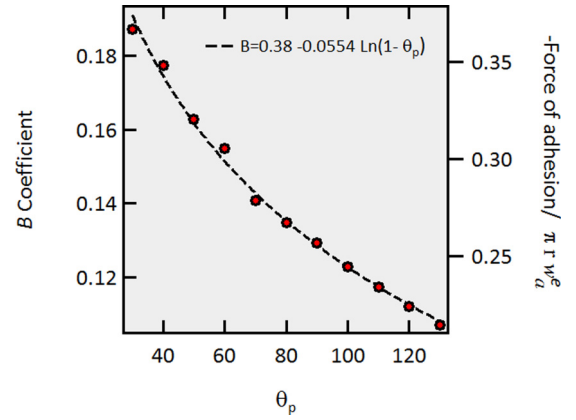


FIG. 12. Force of adhesion on a perfectly solvophobic surface.  $B$  coefficient (left) and scaled force of adhesion (right) for a fixed grip configuration using the approximation  $\beta = 2.5$  [Eq. (36)]. The dashed line is the best fit to a logarithmic dependence of  $B$  on  $\theta_p$ .

of Young's moduli of the elastic solids bodies involved in both the JKR and the Derjaguin models.

Figure 12 shows that the  $B$  coefficient of Eq. (36) is actually a function of  $\theta_p$ . A “deep” drop of  $\theta_p = 120^\circ$  presents half as little adhesion as a comparatively shallow one with  $\theta_p = 30^\circ$  of the same radius. The dashed line in Fig. 12 is the best approximation to a logarithmic dependence of the force of adhesion on  $\theta_p$ . In the limit when  $\theta_p \rightarrow 0^\circ$ ,  $B = 0.38 \approx 0.4$ , and  $F_{ad} \approx -(4/5)\pi r w_a^e$ . Thus, the stiffest possible semidrop in this model still yields a force of adhesion that is smaller than the one obtained in the presence of capillary necks [Eq. (31)] evidencing the relevance of these structures for realistic supersolvophobic surfaces.

### C. Experimental results

In this section we describe the force of adhesion experiments performed on a supersolvophobic system and apply the results of the model and method proposed above to extract the value of the work of adhesion from the experimental results. We perform force of adhesion (or tack) experiments between a 350  $\mu\text{m}$  radius mercury semidrop on a nano-patterned diamond surface [5]. This surface naturally contains structures on both the micron and the nanoscales [Fig. 1(a)] [24]. As a result, there is loss of contact angle hysteresis with mercury concomitant with a very large apparent contact angle greater than  $175^\circ$  [Fig. 1(b)]. To measure the force between this surface and liquid mercury, a thin piece of glass is covered with a sticky polymer (PSA from 3M, USA) and glued to the free end of an optical fiber which points to a quadrant detector. The polymer-covered glass is then placed in contact with a pool of triple distilled mercury and subsequently retracted, leaving a semidrop of the liquid metal strongly pinned on the surface with  $\theta_p$  between  $110^\circ$  and  $120^\circ$  (see sketch in Fig. 2). It was verified that during the experiments the drop remained pinned on its original position. An 830 nm pigtailed solid state laser is connected to the fiber optic, and the deflection of its free end is measured through the signal the quadrant detector (Fig. 2). The fiber-plus-glass-holder system is calibrated by monitoring the changes in resonant frequency vs mass of the

mercury drop. The force is then proportional to the deflection of the fiber (spring constant  $k = 5.4 \text{ N m}$ ). Note this constitutes a “constant grip” configuration since the force exerted by the fiber is not constant but is a function of its deflection. Since Hg is a hazardous material, special care was taken when handling and disposing of it. To measure the force of adhesion, the nanopatterned surface is moved against the drop a certain distance ranging from 5 to 30  $\mu\text{m}$ , then is left to equilibrate for 30 s after which it is finally retracted until detachment occurs. The maximum force measured upon detachment is the force of adhesion. As shown in Fig. 1(c), this force of adhesion is independent of the surface displacement, and its average value is close to 0.5  $\mu\text{N}$  [Fig. 1(c)]. This constancy with respect to compression supports our assumption that the pinning points between Hg and this surface are indeed weak and thus validates our model.

Given that, in Sec. III A, Fig. 9, we obtained the force of adhesion for a semidrop of the same dimensions and  $\theta_p$ , we can compare directly with our experimental results. According to the inset of Fig. 9, a force of adhesion of 0.5  $\mu\text{N}$  corresponds to a contact angle of  $178^\circ$ . Also, from Eq. (31), the effective energy in this case is  $w_a^e = 0.45 \text{ mJ m}^2$ . Measuring this extremely large contact angle would have been very difficult with other methods. This case serves as an example of the use of force of adhesion measurements to quantify the interaction in supersolvophobic systems.

#### IV. SUMMARY AND CONCLUSIONS

We have developed a method to calculate the force of adhesion on both super and perfectly solvophobic surfaces in the presence of weak pinning points. For the particular case explored ( $\theta_p = 110^\circ$ ) the force of adhesion has the same functional form as the result from the Derjaguin model of the adhesion of elastic solids in the constant grip configuration. The peculiar mechanical properties of capillary necks that form during the process of detachment are responsible for a fivefold increase in the force of adhesion as compared to the ideal perfectly solvophobic case.

Given the linear dependence of the force of adhesion on the surface energy, we propose the use of this force to measure surface interactions on supersolvophobic surfaces instead of contact angle measurements [5,7]. Ideal candidates to test our results are superhydrophobic surfaces based on metal hydroxides for which  $\theta^* = 178^\circ$  [38] and superoleophobic ones based on organosilanes ( $\theta^* > 172^\circ$  [39]).

It would be interesting to calculate the force of adhesion vs  $\theta^*$  for a whole range of values of  $\theta_p$ , which can be performed following the method we have developed. This would be equivalent to finding the dependence of the force on the normalized volume of the drop, a parameter normally used in the context of capillary bridges. Finally, the algebraic expression for the asymptotic behavior of the excess area that we find [Fig. 5(c)], makes it possible to obtain, at least in principle, an analytical expression for the force of adhesion arising from capillary necks using the formalism of fracture mechanics [17,19].

An important kind of stability not considered in the present paper is the effect on the drop shape of disturbances of certain constraining parameters, such as volume, pressure, and the position of the pinned line on the backing surface [40–42]. This work is underway.

Finally, we point out that the robustness of the experimental force of adhesion found with respect to pressure [or equivalently with respect to preload, Fig. 1(c)] is very likely due to the extremely high surface tension of liquid mercury. The transition from a Cassie-Baxter state to a Wenzel one (at a critical pressure) as well as the existence of metastable states in the presence of nanoprotusions and the corresponding energy barriers would have to be carefully considered if other liquids of smaller surface tension, such as water were to be used instead [43–46].

#### ACKNOWLEDGMENTS

We gratefully acknowledge funding from CONACYT Projects No. CB-2013-221235-F and No. CB-177679 and from DGAPA-UNAM Projects No. IA-101216 and No. IN-110414. We also thank Cristina Garza for technical assistance.

- 
- [1] B. Derjaguin, *Kolloid-Z.* **69**, 155 (1934).
  - [2] K. L. Johnson, K. Kendall, and A. D. Roberts, *Proc. R. Soc. London, Ser. A* **324**, 301 (1971).
  - [3] D. Bonn, J. Eggers, J. Indekeu, J. Meunier, and E. Rolley, *Rev. Mod. Phys.* **81**, 739 (2009).
  - [4] P. G. de Gennes, F. Brochard-Wyart, and D. Quéré, *Capillarity and Wetting Phenomena* (Springer, New York, 2002).
  - [5] J. V. Escobar and R. Castillo, *Phys. Rev. Lett.* **111**, 226102 (2013).
  - [6] H. J. Butt, I. V. Roisman, M. Brinkmann, P. Papadopoulos, D. Vollmer, and C. Semprebon, *Curr. Opin. Colloid Interface Sci.* **19**, 343 (2014).
  - [7] B. Samuel, H. Zhao, and K. Y. Law, *J. Phys. Chem. C* **115**, 14852 (2011).
  - [8] C. Delauney, *J. Math. Pures Appl. 1er Ser.* **6**, 309 (1841).
  - [9] W. B. Haines, *J. Agric. Sci.* **15**, 529 (1925).
  - [10] R. A. Fisher, *J. Agric. Sci.* **16**, 492 (1926).
  - [11] H. J. Butt and M. Kappl, *Adv. Colloid Interface Sci.* **146**, 48 (2009).
  - [12] A. T. Paxson and K. K. Varanasi, *Nat. Commun.* **4**, 8 (2013).
  - [13] R. Dufour, P. Brunet, M. Harnois, R. Boukherroub, V. Thomy, and V. Senez, *Small* **8**, 1229 (2012).
  - [14] E. J. De Souza, L. C. Gao, T. J. McCarthy, E. Arzt, and A. J. Crosby, *Langmuir* **24**, 1391 (2008).
  - [15] A. B. D. Cassie and S. Baxter, *Trans. Faraday Soc.* **40**, 546 (1944).
  - [16] H. Hertz, *J. Reine Angew. Math.* **92**, 156 (1881).
  - [17] D. Maugis, *J. Colloid Interface Sci.* **150**, 243 (1992).
  - [18] E. Barthel, *J. Phys. D: Appl. Phys.* **41**, 163001 (2008).
  - [19] A. A. Griffith, *Philos. Trans. R. Soc. London, Ser. A* **221**, 163 (1920).
  - [20] R. N. Wenzel, *Ind. Eng. Chem.* **28**, 988 (1936).
  - [21] A. Lafuma and D. Quere, *Nat. Mater.* **2**, 457 (2003).
  - [22] B. N. J. Persson and E. Tosatti, *J. Chem. Phys.* **115**, 5597 (2001).

- [23] M. Ruths, N. A. Alcantar, and J. N. Israelachvili, *J. Phys. Chem. B* **107**, 11149 (2003).
- [24] J. V. Escobar, C. Garza, J. C. Alonso, and R. Castillo, *Appl. Surf. Sci.* **273**, 692 (2013).
- [25] J. F. Joanny and P. G. de Gennes, *J. Chem. Phys.* **81**, 552 (1984).
- [26] M. Delmas, M. Monthieux, and T. Ondarçuhu, *Phys. Rev. Lett.* **106**, 136102 (2011).
- [27] J. B. Keller and G. J. Merchant, *J. Stat. Phys.* **63**, 1039 (1991).
- [28] W. Helfrich, *Zeitschrift für Naturforschung C* **28**, 693 (1973).
- [29] E. J. De Souza, M. Brinkmann, C. Mohrdieck, and E. Arzt, *Langmuir* **24**, 8813 (2008).
- [30] L. Bocquet, E. Charlaix, S. Ciliberto, and J. Crassous, *Nature (London)* **396**, 735 (1998).
- [31] C. H. Mastrangelo and C. H. Hsu, *J. Microelectromech. Syst.* **2**, 33 (1993).
- [32] J. Colchero, A. Storch, M. Luna, J. Gomez-Herrero, and A. M. Baro, *Langmuir* **14**, 2230 (1998).
- [33] L. Zitzler, S. Herminghaus, and F. Mugele, *Phys. Rev. B* **66**, 155436 (2002).
- [34] T. I. Vogel, *SIAM J Appl. Math.* **49**, 1009 (1989).
- [35] W. C. Carter, *Acta Metall.* **36**, 2283 (1988).
- [36] M. A. Fortes, *J. Colloid Interface Sci.* **88**, 338 (1982).
- [37] Y. W. Su, B. H. Ji, Y. G. Huang, and K. H. Hwang, *J. Mater. Sci.* **42**, 8885 (2007).
- [38] E. Hosono, S. Fujihara, I. Honma, and H. S. Zhou, *J. Am. Chem. Soc.* **127**, 13458 (2005).
- [39] J. P. Zhang and S. Seeger, *Angew. Chem., Int. Ed.* **50**, 6652 (2011).
- [40] J. C. Baret, *Morphological Transitions in Simple Electrocapillary Systems: Tools for Microfluidic Liquid Manipulation* (University of Twente, Enschede, Netherlands, 2005).
- [41] J. B. Bostwick and P. H. Steen, *Annu. Rev. Fluid Mech.* **47**, 539 (2015).
- [42] B. J. Lowry and P. H. Steen, *Proc. R. Soc. London, Ser. A* **449**, 1937 (1995).
- [43] A. Giacomello, M. Chinappi, S. Meloni, and C. M. Casciola, *Phys. Rev. Lett.* **109**, 226102 (2012).
- [44] A. Checco, B. M. Ocko, A. Rahman, C. T. Black, M. Tasinkevych, A. Giacomello, and S. Dietrich, *Phys. Rev. Lett.* **112**, 216101 (2014).
- [45] Q. S. Zheng, Y. Yu, and Z. H. Zhao, *Langmuir* **21**, 12207 (2005).
- [46] W. Ren, *Langmuir* **30**, 2879 (2014).